Pore-scale imaging of displacement patterns in an altered-wettability carbonate

Qingyang Lin [a,b,*], Branko Bijeljic [b], Sajjad Foroughi [b], Steffen Berg [c], Martin J. Blunt [b]

[a] State Key Laboratory of Clean Energy Utilization, State Environmental Protection Engineering Center for Coal-Fired Air Pollution Control, Zhejiang University, Hangzhou 310027, China
[b] Department of Earth Science and Engineering, Imperial College London, London SW7 2AZ, United Kingdom
[c] Shell Global Solutions International B.V., Grasweg 31, 1031 HW Amsterdam, the Netherlands

HIGHLIGHTS

- In this oil-wet carbonate, micro-porosity plays a crucial role in flow connectivity.
- The displacement is characterised by a thermodynamic contact angle of 120°.
- The flow behaviour is different from a mixed-wet sandstone with angle close to 95°.
- The carbonate case has a high brine rel-perm and a large/negative capillary pressure.

ARTICLE INFO

ABSTRACT

High-resolution X-ray imaging combined with a steady-state flow experiment is used to demonstrate how pore-scale displacement affects macroscopic properties in an altered-wettability microporous carbonate, where porosity and fluid saturation can be directly obtained from the grey-scale micro-CT images. The resolvable macro pores are largely oil-wet with an average thermodynamic contact angle of 120°. The pore-by-pore analysis shows locally either oil or brine almost fully occupied the macro pores, with some oil displacement in the micro-porosity. We observed a typical oil-wet behaviour consistent with the contact angle measurement. The brine tended to occupy the larger macro pores, leading to a higher brine relative permeability, lower residual oil saturation, than under water-wet conditions and in a mixed-wet sandstone. The capillary pressure was negative and seven times larger in the carbonate than the sandstone, despite having a similar average pore size. These different displacement patterns are principally determined by the difference in wettability.

© 2021 The Author(s). Published by Elsevier Ltd. This is an open access article under the CC BY-NC-ND license (http://creativecommons.org/licenses/by-nc-nd/4.0/).

1. Introduction

In recent years, X-ray microtomography has been widely used in combination with flow experiments to improve our understanding of multiphase flow in porous media by visualizing pore structure and multiphase flow within the pore space (Blunt, 2017). In particular, by using advanced imaging techniques and image processing algorithms, it is now possible to visualize and quantify pore-scale displacement processes and measure flow properties in complex porous systems, including capturing saturation below the image resolution (Boone et al., 2014; Leu et al., 2014; Lin et al., 2016; Saxena et al., 2017; Soulaine et al., 2016); wettability characterization by directly measuring geometric contact angles (AlRatrout et al., 2018, 2017; Andrew et al., 2014a; Prodanović et al., 2004), using topological approaches (Blunt et al., 2020; Sun et al., 2020), and thermodynamic contact angles (Akai et al., 2020; Blunt et al., 2019); interfacial properties (Andrew et al., 2014b; Armstrong et al., 2012b; Culligan et al., 2006; Garing et al., 2017; Li et al., 2018; Lin et al., 2019b, 2017); and the dynamics of displacement and reactive transport (Al-Khulaifi et al., 2017; Berg et al., 2013; Jackson et al., 2020; Pak et al., 2015; Singh et al., 2017).

In previous studies, we have established an imaging-based experimental workflow to fully quantify two-phase flow properties by measuring relative permeability, capillary pressure and contact angles simultaneously (Alhammadi et al., 2020; Blunt et al., 2019; Gao et al., 2017; Lin et al., 2019b, 2018). In an altered-wettability

---

* Corresponding author at: State Key Laboratory of Clean Energy Utilization, State Environmental Protection Engineering Center for Coal-Fired Air Pollution Control, Zhejiang University, Hangzhou 310027, China.
   E-mail address: qingyang_lin@zju.edu.cn (Q. Lin).

system we observed well-connected fluid phases and the oil-brine interfaces had a negative Gaussian curvature indicating that the two principal curvatures had opposite signs (Alhammadi et al., 2020; Lin et al., 2019b). In particular, we observed minimal surfaces, with a very low mean curvature, with two approximately equal, but opposite principle curvatures in a Bentheimer sandstone and used this observation to explain the favourable displacement efficiency (Lin et al., 2019b).

In this work we will investigate if the same behaviour - minimal surfaces and favourable displacement – are seen in a dual-porosity carbonate that has undergone a wettability alteration. In this case there are two significant differences compared a sandstone, which, as we show later, will have a controlling effect on the measured macroscopic flow properties. Firstly, carbonates, in general, tend to undergo a stronger wettability alteration after contact with crude oil compared to sandstones, although this also depends on the oil and brine composition as well as the temperature and pressure conditions (Morrow and Buckley, 2011). Secondly, carbonates are frequently characterized by a significant fraction of micro-porosity. This micro-porosity often remains largely brine saturated and provides additional connectivity for the brine phase, so that it can flow and connect readily through the pore space. This overall leads to a lower displacement efficiency and less favourable recoveries (Blunt, 2017).

In this study, we performed a similar steady-state fractional flow experiment as that on Bentheimer sandstone (Lin et al., 2019b) but on an Estaillades carbonate sample with a significant amount of micro-porosity. We introduced a new image analysis method which can be used to determine porosity and fluid saturation without performing image segmentation, which could be uncertain due to the existence of both oil and brine phases in the pore space at the same time. We perform a pore-by-pore imaging-based analysis and compare the results with those obtained from the water-wet Estaillades carbonate (Gao et al., 2019) and the mixed-wet Bentheimer sandstone experiment. In particular, we will ascertain the impact of complex geometry and wettability on macroscopic flow properties through the characterization of saturation, pressure response and relative permeability, combined with an analysis of interfacial properties including interfacial area, contact angles and curvatures. Our overall objective is to use pore-scale descriptors to link pore-by-pore image analysis to macroscopic multiphase flow behaviour. We will demonstrate how a stronger wettability alteration and the presence of micro-porosity leads to more oil-wet behaviour compared to similar experiments in sandstones, and discuss the implications for storage and recovery processes.

The key contributions of this work are three-fold: (i) the determination of saturation and porosity in a micro-porous carbonate without image segmentation; (ii) a pore-scale investigation of occupancy and wettability coupled with macroscopic measurements of capillary pressure and relative permeability on an oil-wet carbonate; and (iii) a physical explanation for the oil-wet-type behaviour observed, in contrast to previous studies on water-wet and mixed-wet samples.

2. Materials and methods

2.1. Sample preparation

The rock sample was Estaillades carbonate with an average porosity of 0.294 ± 0.006 obtained from mercury injection (measured by Autopore 9520, Micromeritics) on a twin sample. Two cylindrical samples with 6.1 mm diameter and length 17.6 and 26.0 mm were saturated with formation brine (12.69 wt% NaCl, 5.32 wt% $CaCl_2 \cdot 2H_2O$, and 2.72 wt% $MgCl_2 \cdot 6H_2O$), followed by cen-

trifugation (equivalent capillary pressure of 20 kPa) with decalin (cis and trans decahydronaphthalene mixture) to initialize the sample with a brine saturation (S_{wi}) of 0.581 ± 0.017. Note the high initial water saturation compared to values of approximately 0.1 in sandstone experiments using similar preparation protocols (Lin et al., 2019b, 2019c): here a significant fraction of the micro-porosity remains brine saturated. The decalin in the sample was then exchanged with a Middle-Eastern crude oil (TAN = 0.07 mg KOH/g, TBN = 0.084 mg/g, SARA analysis: Saturates = 58.45, Aromates = 36.92, Resins = 4.36, Asphaltenes = 0.28, density = 830 k g/m³, viscosity = 4–6 mPa.s at room temperature). The two samples were kept in the crude oil for four weeks at 80 °C temperature and 3 MPa pressure to alter the wettability (Lin et al., 2019c, 2019b). Then the crude oil in the samples was first replaced by decalin and then further replaced by n-decane (viscosity = 0.838 mPa.s provided by PubChem, open chemistry database) to conduct the flow experiment. The brine solution injected into the sample in the flow experiment is sodium iodide (NaI) doped brine (containing 7 wt% NaI, 12.69 wt% NaCl, 5.32 wt% $CaCl_2 \cdot 2H_2O$, and 2.72 wt% $MgCl_2 \cdot 6H_2O$; the viscosity of the brine was measured as 1.20 ± 0.02 mPa·s at 20 °C).

2.2. Experimental procedure

The two cores were placed in series (the shorter one was placed closer to the injection side, followed by the longer sample). The whole core assembly was placed in a Hassler type flow cell made of carbon fibre epoxy with low X-ray photon attenuation. Brine and decane were injected simultaneously into the system at different fractional flows, the ratio of the volumetric brine flow rate to the total flow rate of oil and brine ($f_w = 0, 0.05, 0.25, 0.5, 0.75, 0.9, 1$) with a constant total flow rate of 0.02 ml/min. For each fractional flow, the injection occurred over a period of at least 12 h to ensure that a steady-state condition was reached, which was checked by the differential pressure measured by a high accuracy transducer (Keller PD-33X transducer, with an accuracy of ± 0.5 kPa). The interfacial tension between brine and decane was measured to be 47.1 ± 1.5 mN/m, at ambient conditions measured by the pendant drop method (Rame-Hart 590 F4 series) (Andreas et al., 1937; Stauffer, 1965). The detailed experimental procedure could be found in our previous study (Lin et al., 2019b).

For each fractional flow, after steady-state was reached, the centre part of the longer sample (closer to the production end), with a total length of 12.88 mm (voxel size of 3.58 μm) was imaged using a Zeiss Versa 510 X-ray microscope with a flat panel detector. All the images were registered to have the same orientation, followed by applying a nonlocal means edge preserving filter (Buades et al., 2008) for noise reduction, and finally segmented into three phases (brine in the macro pores, oil in the macro pores, and the rest including solid phase and sub-resolution micro-porosity containing fluids) using a seeded watershed algorithm (Andrew et al., 2014b; Jones et al., 2007; Schlüter et al., 2014). The image dimension of the entire field of view is $5.01 \times 5.01 \times 12.88$ mm ($1400 \times 1400 \times 3600$ voxels). An example image is shown in Fig. 1.

3. Results and discussion

We first characterize the pore structure of the Estaillades carbonate, focusing on the impact of sub-resolution micro-porosity and the connectivity of the macro pores (Section 3.1). We then quantify saturation (Section 3.2), study the filling sequence (Section 3.3), analyse wettability (Section 3.4), calculate interfacial area (Section 3.5), and present curvature, capillary pressure and Gaus-
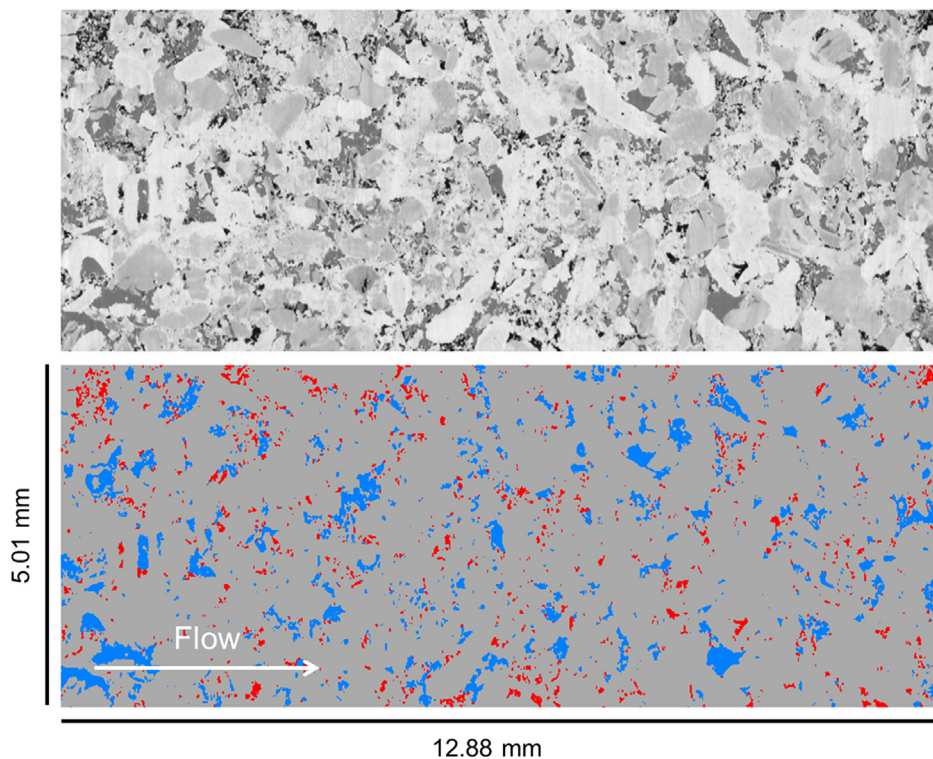
Fig. 1. (Top) Grey-scale two-dimensional cross-sections of a three-dimensional image at $f_w = 0.5$ after applying a nonlocal means edge preserving filter. The dimension of the image is $1400 \times 1400 \times 3600$ voxels with a $3.58\ \mu m$ voxel size. (Bottom) The image was segmented into three phases showing brine in the macro pores (blue), oil in the macro pores (red) and the remaining phases including solid phase and sub-resolution micro-porosity containing fluid phases (grey). (For interpretation of the references to colour in this figure legend, the reader is referred to the web version of this article.)

sian curvatures (Section 3.6). Finally, we show the relative permeabilities and provide insights on how pore-scale properties affect macroscopic flow properties with a discussion of implications for recovery (Section 3.7).

3.1. Characterization of pore structure

We used a network extraction tool (Dong and Blunt, 2009; Raeini et al., 2017) to identify individual pores from an image. A pore is defined as a wide region of the pore space, separated from other pores by a bounding surface, a throat, which represents a restriction in the pore space. The pore radius is the radius of the largest sphere that can fit entirely in the pore, while the throat radius is the radius of the largest sphere centred on the throat. We can divide the pore space into individual pore regions: every pore voxel in the image is assigned to a unique pore. This division can only be performed for the macro pores, which are explicitly resolvable in the image: sub-resolution micro-porosity cannot be considered in this analysis.

We also compared the pore and throat radius distributions for both Estaillades carbonate and Bentheimer sandstone, shown in Fig. 2. There is no significant difference in these distributions, indicating similar pore and throat sizes for the resolvable macro pores. However, the ratio of the number of throats to pores, which is half the coordination number, is only 0.70 for Estaillades carbonate, while it is 2.25 for Bentheimer sandstone, indicating that the macro pores are much less connected for the carbonate. In addition, this reduced pore connectivity can also be seen by plotting the number of pores and throats which are not connected through macro pores, which implies that they are only connected through pores and throats below the image resolution, and the distribution of coordination number for both cases. The coordination number for all the pores is plotted in Fig. 3. For the carbonate, there is a

large fraction of macro pores having a zero coordination number. The pore space therefore only remains connected through sub-resolution micro-porosity, which is largely absent in the sandstone.

The conclusion of this section is that the carbonate is less connected through macro pores than the sandstone; instead connectivity is maintained through micro-porosity. How this affects the flow behaviour and pore-scale displacement is presented in the subsequent sections.

3.2. Saturation

The grey-scale values were directly used to calculate the fluid saturation – we did not used segmented images for this purpose. The advantage of this approach is that it avoids uncertainties associated with the segmentation, particularly for this case where 60% of the porosity is contained in sub-resolution pores containing different fluid phases where complex segmentation using differential imaging is needed (Alhammadi et al., 2020; Gao et al., 2019; Jackson et al., 2020; Lin et al., 2016).

The average porosity was obtained as follows:

$$\phi = \frac{CT_{brine} - CT_{air}}{CT_{brine,ref} - CT_{air,ref}} \tag{1}$$

where CT_{brine} is the average grey-scale value for the sample saturated with brine, CT_{air} is the average grey-scale value of the dry sample that only contains air, $CT_{brine,ref}$ is the representative grey-scale value for the brine phase, and $CT_{air,ref}$ is the grey-scale value for the air phase. The calculated porosity was 0.288 ± 0.013 which agrees within experimental uncertainty with the independent measurement using mercury injection on a twin sample of 0.294 ± 0.006.
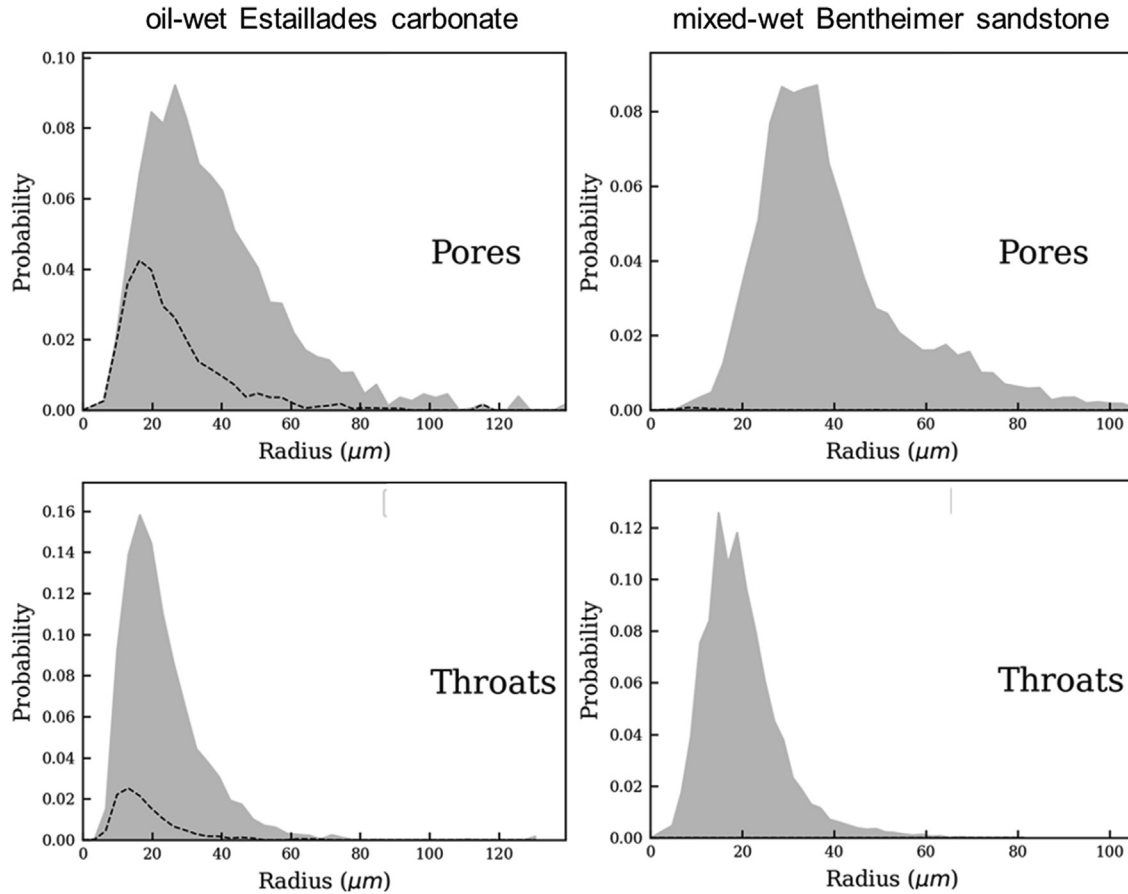
Fig. 2. The number of macro pores and throats comparing our Estaillades carbonate (pores 104,241; throats 72,506) and Bentheimer sandstone (pores 97,798; throats 220,272). The dashed lines show macro pores that are only connected through pores and throats below the image resolution. The grey areas represent the size distribution for all the macro pores and throats.
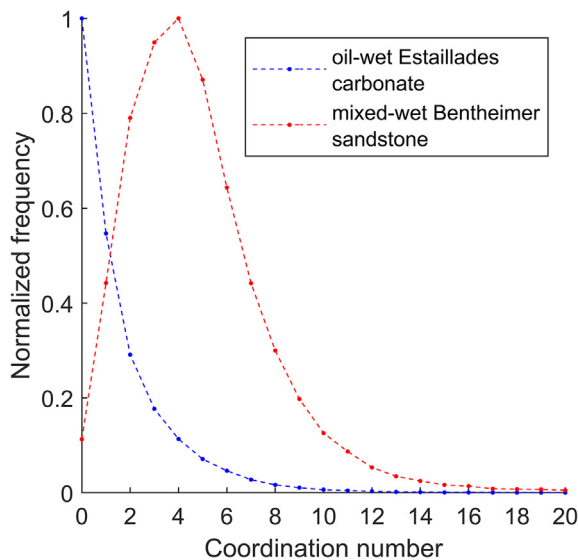

Fig. 3. Histogram of the coordination number comparing the carbonate and sandstone, showing poor connectivity through macro pores for the micro-porous carbonate.

Using a similar concept, the brine saturation at each fractional flow ($S_{w,fw}$) was also calculated:

$$S_{w,fw} = 1 - \frac{CT_{brine} - CT_{fw}}{CT_{brine} - CT_{oil}} \qquad (2)$$

where CT_{brine} is the average grey-scale value for the sample saturated with brine, CT_{fw} is the average grey-scale value for the sample partially saturated with brine and oil at each fractional flow scan, CT_{oil} is the average grey-scale value for the sample saturated with oil.

Fig. 4 shows the porosity variation along the sample, as well as the brine saturation profile including the overall brine saturation, brine saturation in macro pores, and brine saturation in sub-resolution micro pores. Because of differences in the brine salinity during wettability alteration and the experiments (see Section 2.1), we were unable to obtain a saturation profile for $f_w = 0$ directly from imaging. Approximately 60% of the porosity is contributed by sub-resolution porosity. It is evident that initially oil occupies most of the macro pores but also a significant amount of the sub-resolution micro-porosity. This oil is displaced from both the macro and micro pores as the fractional flow is increased.

3.3. Pore occupancy

By using the extracted pore labels generated by pore network extraction (described in Section 3.1), we computed the brine fraction in the macro pores for all fractional flows, shown in Fig. 5. For Estaillades carbonate, the proportion of brine in most of the pores is either smaller than 10% or higher than 90%, in contrast to Bentheimer sandstone, where many more pores have a fractional occupancy. This indicates that layers of oil and brine are rarely present in the larger carbonate pores: at the resolution of the image most pores appear to be almost completely brine or oil filled with con-
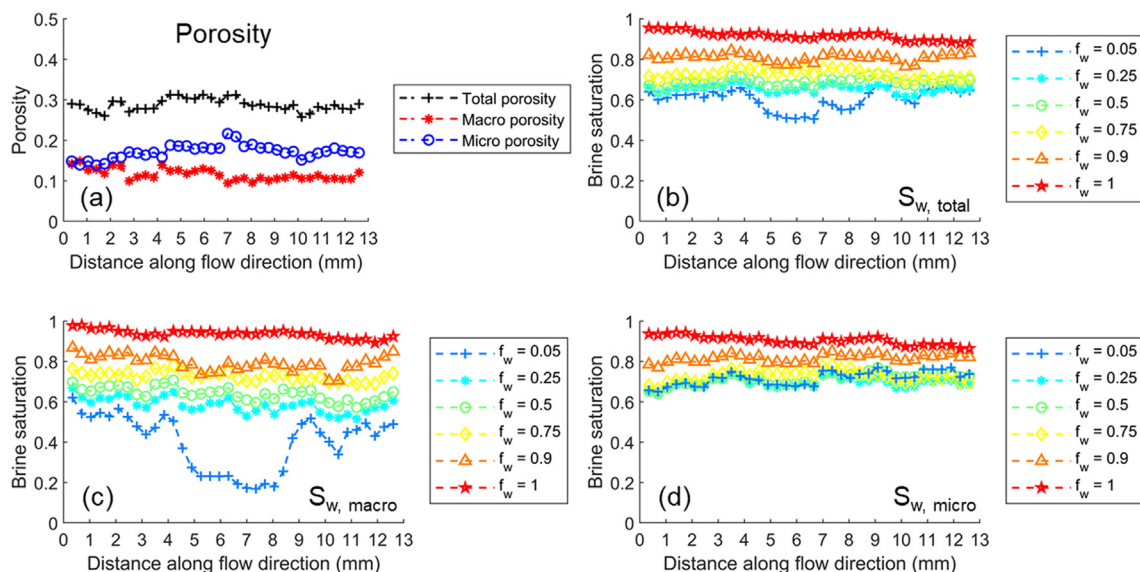
Fig. 4. Porosity and saturation profiles along the sample. (a) porosity; (b) the overall brine saturation; (c) brine saturation in macro pores; (d) brine saturation in sub-resolution micro pores.
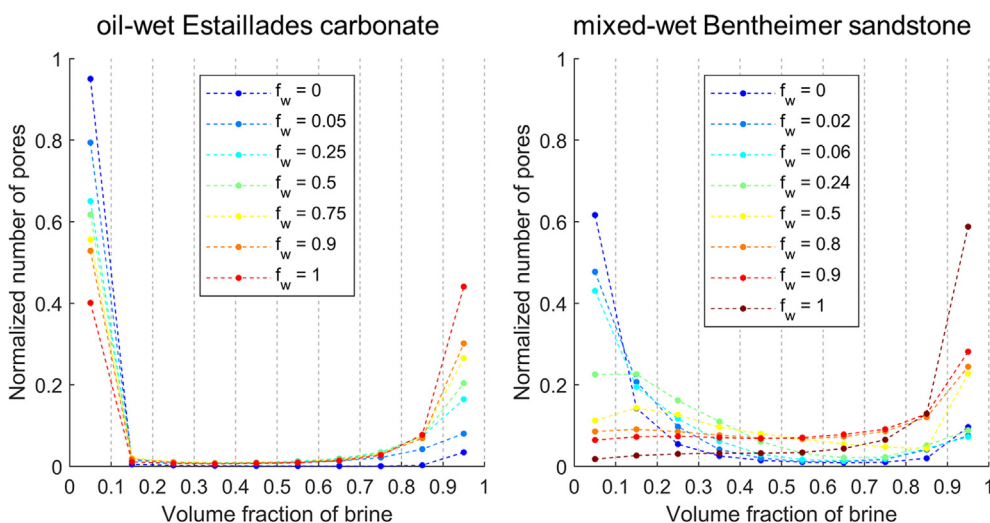

Fig. 5. Histogram of the number of macro pores against the fraction of the pore volume occupied by brine comparing our carbonate sample (macro pores only) in this study and a mixed-wet sandstone.

nectivity maintained through sub-resolution micro-porosity in which there is also displacement, as shown in Fig. 4d.

To further quantify pore occupancy, we calculated the fraction of oil-filled voxels in the largest sphere at the centre of each pore and throat. We define a pore to be oil filled if the oil fraction is larger than 50%: the results are shown in Fig. 6.

During displacement, there is a clear tendency for the largest pores and throats to be preferentially filled with brine in the carbonate, while oil remains in the smaller elements. This indicates that the sample is oil-wet, which will be explored further in the next section: the larger macro pores are filled first followed by successively smaller elements. This is quantified by plotting the histogram of oil-filled pores whose occupancy changed to become brine-filled between each fractional flow step, Fig. 7: we see that at the beginning of the displacement it is the larger oil-filled elements that are filled with water, again consistent with oil-wet conditions.

However, for the sandstone, we observed filling of pores and throats of all size throughout the displacement. This indicates that there is a mix of water-wet elements with contact angles below 90° – where the smaller ones are filled preferentially – and oil-wet regions with contact angles above 90° whose larger pores and throats fill first (Lin et al., 2019b).

To summarize, displacement in the macro pores of the carbonate proceeds largely in order of size, with the largest pores and throats filled first. This type of filling sequence has also been observed from time-resolved synchrotron imaging on oil-wet reservoir carbonate (Alhosani et al., 2020). This is characteristic of an oil-wet rock, whereas in the sandstone, elements of all size are filled throughout waterflooding with no clear size segregation. A similar filling of pores of all size has also been observed in an altered-wettability quarry carbonate (Scanziani et al., 2020). In the next section we will confirm this understanding through the measurement of contact angle. The second observation is that
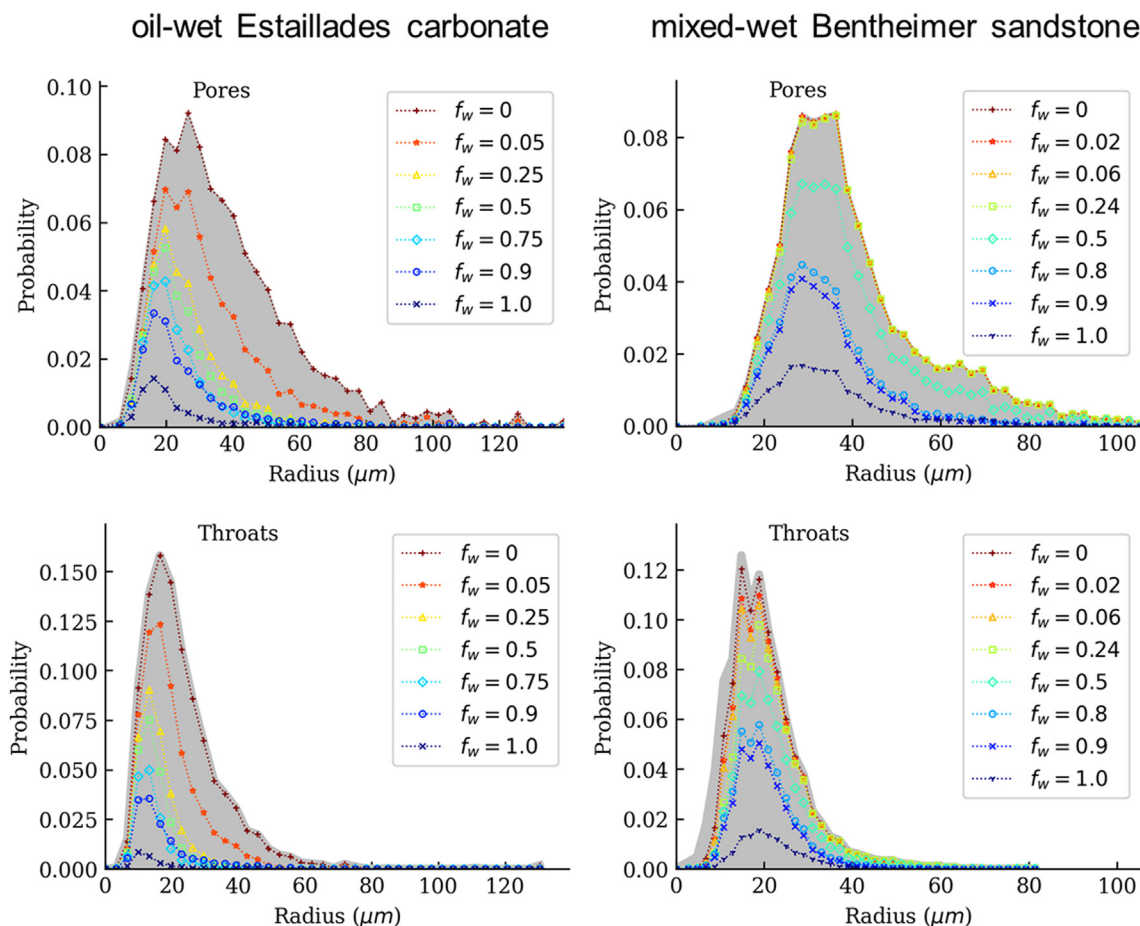
oil-wet Estaillades carbonate   mixed-wet Bentheimer sandstone

Fig. 6. Histogram plot showing distribution of pores and throats filled with oil during brine injection. The grey areas represent the size distribution for all the pores and throats.

the macro pores in the carbonate tend to be almost completely filled with either oil or brine – we do not observe a significant amount of oil and brine in wetting and spreading layers.

3.4. Characterization of wettability

To quantify the interfacial properties and wettability, the voxelized interfaces between two phases (fluid-fluid or fluid-solid) were extracted and smoothed by a boundary preserving surface smoothing algorithm with 150 iterations (Lin et al., 2019b; Taubin, 1995). We then calculated the image saturation in the macro pores, the specific surface area between two phases i and j which is defined as $a_{ij} = A_{ij}/V$ (where A_{ij} is the surface area between two phases and V is the volume of the region of the porous medium under consideration), and the total curvature between two fluid phases, κ, shown in Table 1.

From changes in saturation, interfacial area, and the curvature, we can compute the thermodynamic contact angle, θ_t (Akai et al., 2020; Blunt et al., 2019), to characterize the wettability:

$$\Delta a_{ws} \cos(\theta_t) = \kappa \phi \Delta S_w + \Delta a_{ow} \qquad (3)$$

θ_t is the contact angle, averaged over the sample, that provides the correct energy balance for displacement, ignoring viscous dissipation. It is the average angle to input into pore-scale models that assume quasi-steady-state flow (Blunt et al., 2019).

The details of the interfacial properties are shown in Table 1, and compared with mixed-wet Bentheimer sandstone. We considered the changes in saturation and interfacial areas between experiments at two fractional flows: we were unable to obtain reliable

results for curvature for $f_w = 0$ and 1 and so these were excluded from the analysis. The uncertainty in θ_t is obtained by choosing all possible two steady state pairs and computing the standard deviation of the θ_t values. For the calculation of the term $\phi \Delta S_w$ in Eq. (3) we used the porosity in the macro pores and the change in saturation in the macro pores only: the displacement in micro-porosity was ignored, as we could not estimate the corresponding changes in interfacial areas.

From Table 1, we can see that for the Bentheimer sandstone the average contact angle was approximately 95°, implying mixed-wet conditions, in that locally there are regions of the pore space which are both water-wet and oil-wet with contact angles both above and below 90° (Lin et al., 2019a). Also, the interfacial curvature was close to zero. In contrast, the Estaillades carbonate is more oil-wet with a contact angle of approximately 120°, with a larger negative interfacial curvature.

Contact angles can also be measured directly on the segmented images at the three-phase contact between the two fluids and the solid (AlRatrout et al., 2017; Andrew et al., 2014a). However, as described next, the images showed only tiny regions of contact making any measurement of the geometric contact angle impossible.

3.5. Interfacial area

Fig. 8 shows the interfaces between oil and brine in macro pores comparing the carbonate and sandstone at a similar brine saturation. As visually evident in the figure, the interfacial area between brine and oil phases in the carbonate is much smaller than in the
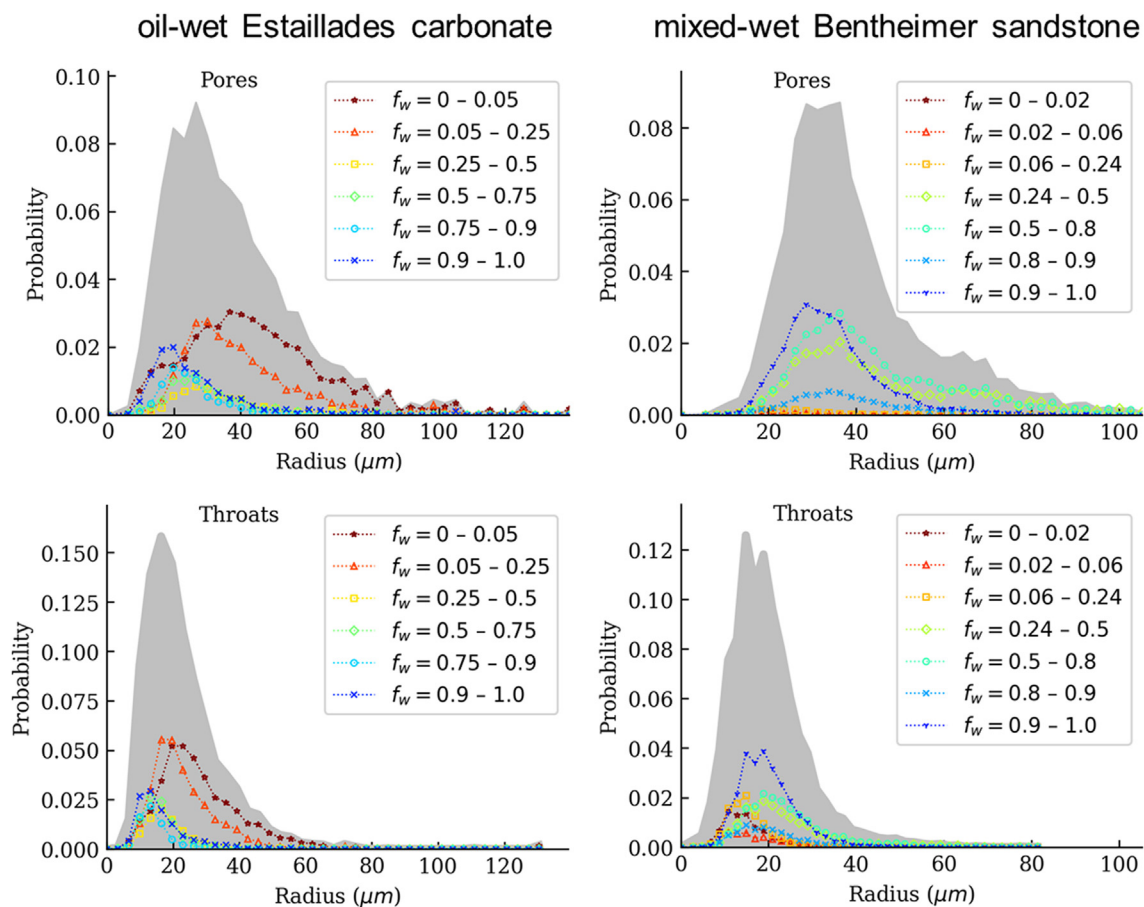
oil-wet Estaillades carbonate

mixed-wet Bentheimer sandstone

Fig. 7. Histogram plot showing distribution of oil-filled pores and throats which changed to be brine-filled during brine injection between two fractional flows. The grey areas represent the size distribution for all the pores and throats.

Table 1
Interfacial properties and computed thermodynamic contact angle θ_t, comparing Estaillades carbonate and Bentheimer sandstone (Lin et al., 2019b).

Case	f_w	S_w[1]	a_{ow}(mm^{-1})	a_{ws}(mm^{-1})	κ (mm^{-1})	P_c(kPa)	θ_t
Estaillades carbonate	0.05	0.401	0.28	2.46	−27.85	−1.31	119.7°±3.2°
	0.25	0.655	0.30	4.54	−35.50	−1.67	
	0.5	0.726	0.26	5.19	−36.59	−1.72	
	0.75	0.810	0.19	6.05	−42.05	−1.98	
	0.9	0.828	0.16	6.39	−44.23	−2.08	
Bentheimer sandstone	0.24	0.320	6.81	23.31	−4.99	−0.26	94.7°±3.9°
	0.5	0.482	7.89	32.92	−5.44	−0.28	
	0.8	0.655	7.22	42.39	−5.05	−0.26	
	0.9	0.700	7.13	45.31	−2.84	−0.15	

[1] Note that for Estaillades, the S_w in the table is the brine saturation in the macro pores only.

sandstone. The fluid-fluid interfaces in the carbonate tended to reside in the narrow restrictions, throats, between wider pore spaces. In Bentheimer sandstone, in contrast, we also resolve oil-brine interfaces within pores, where the oil resides in layers, sandwiched between initial brine in the corners of the pores space and brine in the pore centre (Lin et al., 2019b): these layers are not observed in the carbonate, as shown by the filling analysis of Section 3.3. This implies that the macro pore space – as we quantified in Section 3.1 – is poorly connected. To facilitate displacement there must also be significant flow in micro-porosity.

Fig. 9 shows the oil-brine, oil-solid and brine-solid interfacial areas as a function of saturation. Overall the fluid-solid areas are larger for the sandstone, despite similar average pore sizes. The reason for this is that in the carbonate we only consider the resolvable porosity, which is around 0.11 (see Fig. 4), as opposed to 0.23

in the sandstone. The fraction of the solid contacted by oil, at the same saturation, tends to be slightly higher in the carbonate, consistent with the more oil-wet conditions quantified in the previous section.

3.6. Curvature and capillary pressure

The capillary pressure is calculated using Young–Laplace law (Armstrong et al., 2012a; Lin et al., 2019b, 2018):

$$P_c = \sigma\kappa \tag{4}$$

where σ is the interfacial tension between the brine and oil phases, and κ is the total curvature of the interface. Fig. 10 shows the capillary pressure comparing the carbonate and sandstone samples, using Eq. (4) and the measured interfacial curvatures (the interfa-
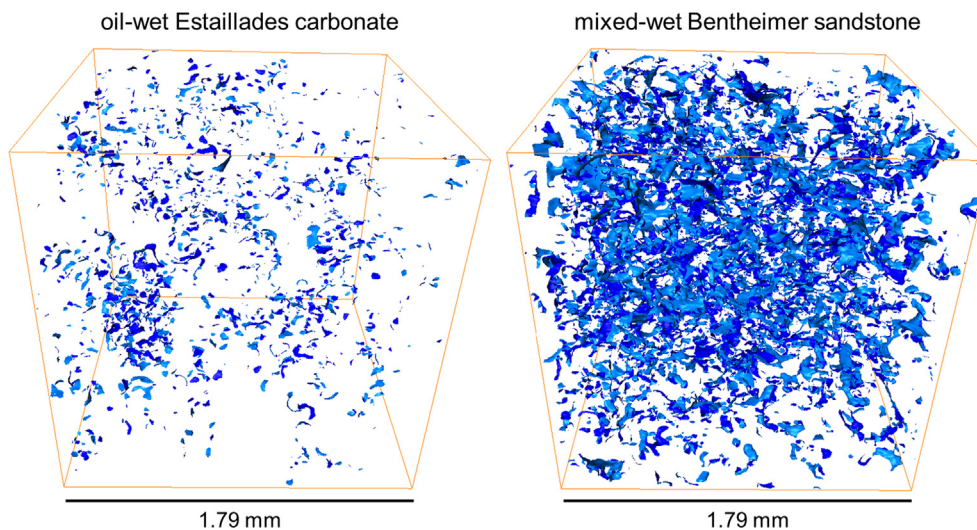
oil-wet Estaillades carbonate   mixed-wet Bentheimer sandstone

Fig. 8. Oil and brine interfaces in the macro pores comparing Estaillades carbonate and Bentheimer sandstone (Lin et al., 2019b). The image for the carbonate ($f_w = 0.25$) has a brine saturation in the macro pores of $S_w = 0.655$. The image for the sandstone (fractional flow $f_w = 0.8$) has a brine saturation in the macro pores of $S_w = 0.655$ as well. Both images have the same dimension of $500 \times 500 \times 500$ voxels (approximately 5.74 mm³).
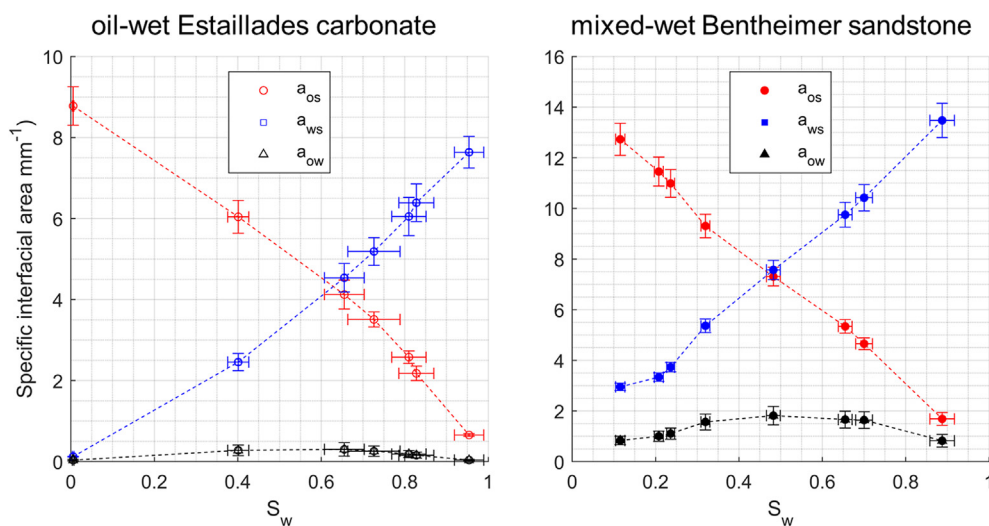

Fig. 9. Specific interfacial area, a, between different phases for Estaillades carbonate and Bentheimer sandstone. The specific surface is defined as the surface area per unit volume. a_{os}, a_{ws} and a_{ow} represent the specific interfacial areas between oil and solid phases (red circles), brine and solid phases (blue squares), and oil and brine phases (black triangles), respectively. Note that for the carbonate, S_w is the brine saturation in the macro pores only. (For interpretation of the references to colour in this figure legend, the reader is referred to the web version of this article.)

cial properties can be found in Table 1). Since the Estaillades carbonate and Bentheimer sandstone have similar macro pore sizes, Fig. 2, it implies that the principal reason for the differences seen in the magnitude of the capillary pressure is the wettability and not pore size. The capillary pressure is negative for the carbonate, consistent with oil-wet conditions, and larger in magnitude than seen in the sandstone. In the carbonate, the interfacial curvature is not close to zero: we do not see the presence of approximately minimal surfaces.

Connectivity can be quantified from the product of the interfacial curvatures in orthogonal directions: the Gaussian curvature shown in Fig. 11. There is a broader distribution than seen for the mixed-wet sandstone with significantly more positive values. Since the total curvature (the sum of the curvatures in orthogonal directions) is negative, giving a negative capillary pressure (see Table 1 and Fig. 10), we can assume that in these cases both curvatures are negative. Again, this is consistent with oil-wet conditions,

with water bulging into oil: water forms ball-shaped structures in the larger pore spaces. As the fractional flow increases, the Gaussian curvature has more positive values, which indicates that the phases become less well connected in the pore space (Berger et al., 2012; Gauss and Pesic, 2005; Lin et al., 2019b).

We have shown that the filling sequence (Section 3.3), contact angles (Section 3.4), oil-solid interfacial areas (Section 3.5), and capillary pressure (Fig. 10) all point to more oil-wet conditions in the carbonate sample than in the sandstone used for comparison. This is the first major difference between the two samples. In addition, as shown in Section 3.1, the carbonate has a much more poorly connected macro porosity, with a lower oil-brine interfacial area (Section 3.5), and larger (positive) Gaussian curvatures (Fig. 11): this means that the flow of multiple phases through the macro pores is constrained and that connectivity can only be maintained through micro-porosity. This is explored quantitatively in the next section where we present relative permeability.
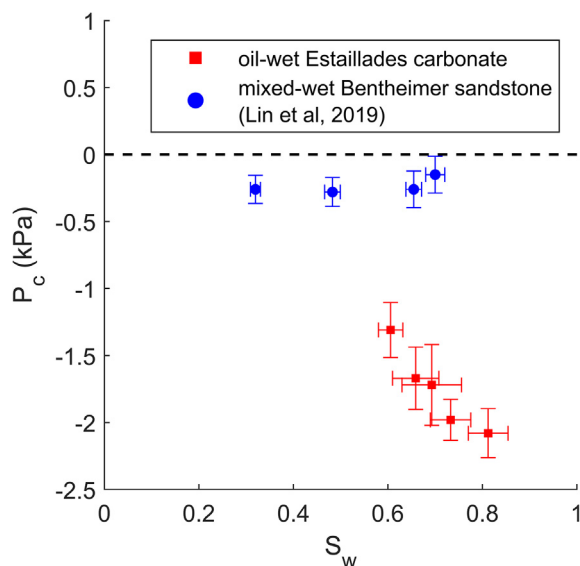
Fig. 10. The capillary pressure for Estaillades carbonate compared to the previously-published results for a mixed-wet Bentheimer sandstone (Lin et al., 2019b) presented in Table 1. The error bars represent the uncertainties of brine saturation and curvature measurements from image analysis.
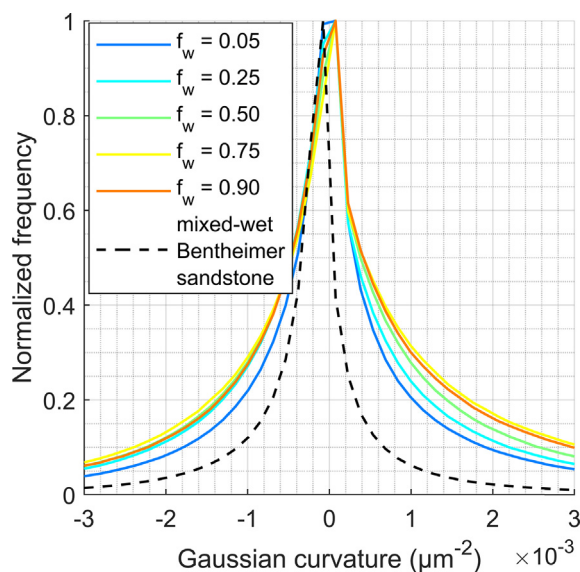

Fig. 11. Comparison of Gaussian curvature between the Estaillades carbonate (macro pores only) and Bentheimer sandstone for $f_w = 0.5$.

3.7. Relative permeability and implications for recovery

With the saturation values computed using Eq. (2) and the differential pressure measurements (shown in Fig. 12), the relative permeability for both the oil and brine phases can be calculated (Blunt, 2017; Lin et al., 2019b, 2018). In this study, we did not observe a clear saturation gradient so we did not apply an analytical correction of the estimated relative permeabilities to account for a possible capillary end effect (Lin et al., 2018).

Compared with previously-published results on a water-wet Estaillades carbonate (Gao et al., 2019), we observe a typical oil-wet behaviour from our experiments, Fig. 13, where the oil relative permeability is lower and the brine relative permeability rises sharply when brine fills the larger pores. In a water-wet medium, the water (brine) preferentially fills the smaller pores, whereas here – as we have shown in Section 3.3 – the water preferentially occupies the larger pores which have a higher flow conductance.

For both the water-wet and altered-wettability Estaillades experiments the initial water saturation is similar – approximately 0.58. This high value is a consequence of the significant volume of sub-resolution micro-porosity in the samples which remains largely water-saturated throughout the experiment. The residual oil saturation ($S_{or} = 0.08$) is lower than in the water-wet case ($S_{or} = 0.14$), while the brine relative permeability at S_{or} ($k_{rw} = 0.48$) is higher than under water-wet conditions ($k_{rw} = 0.27$). Again, this is consistent with good oil connectivity in smaller pores and layers in the altered-wettability case, where the water occupies larger pores. In addition, the cross-over saturation ($S_{w,cross} = 0.68$), where the oil relative permeability equals the brine relative permeability, decreases compared to the water-wet case ($S_{w,cross} = 0.76$), which implies poorer waterflood recovery (Blunt, 2017).

This behaviour is in contrast to that observed in Bentheimer sandstone. Here, as we show in Section 3.3, the macroscopic manifestation of the flow behaviour was more mixed-wet with filling of pores of all size during waterflooding. This led to rather poor water connectivity and a low brine relative permeability, leading to a higher cross-over saturation ($S_{w,cross} = 0.65$). compared to the water-wet conditions ($S_{w,cross} = 0.55$), implying favourable waterflood recovery (Lin et al., 2019b, 2018). Also, as shown in Section 3.6, the capillary pressure is close to zero with interfaces of negative Gaussian curvature, implying well-connected phases, whereas in the oil-wet Estaillades, the capillary pressure is larger (more negative) with more positive Gaussian curvatures, indicating poorer connectivity.

Relative permeability, capillary pressure and pore-scale configurations were also measured on an altered-wettability reservoir carbonate by Alhammadi et al. (2020). In this experiment, the relative permeabilities implied favourable recovery: micro-porosity facilitated the filling of larger macro pores with brine throughout
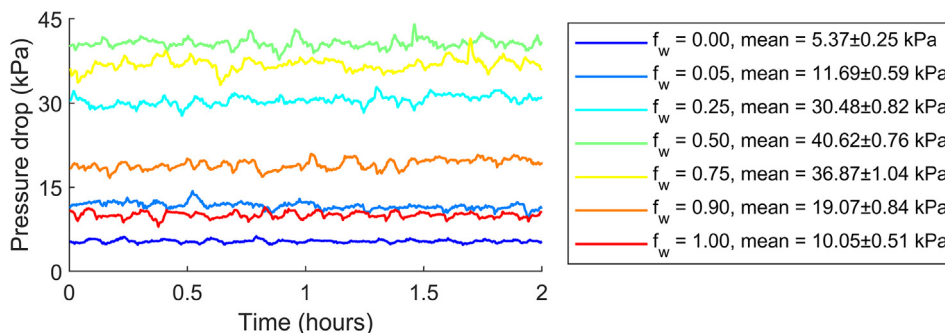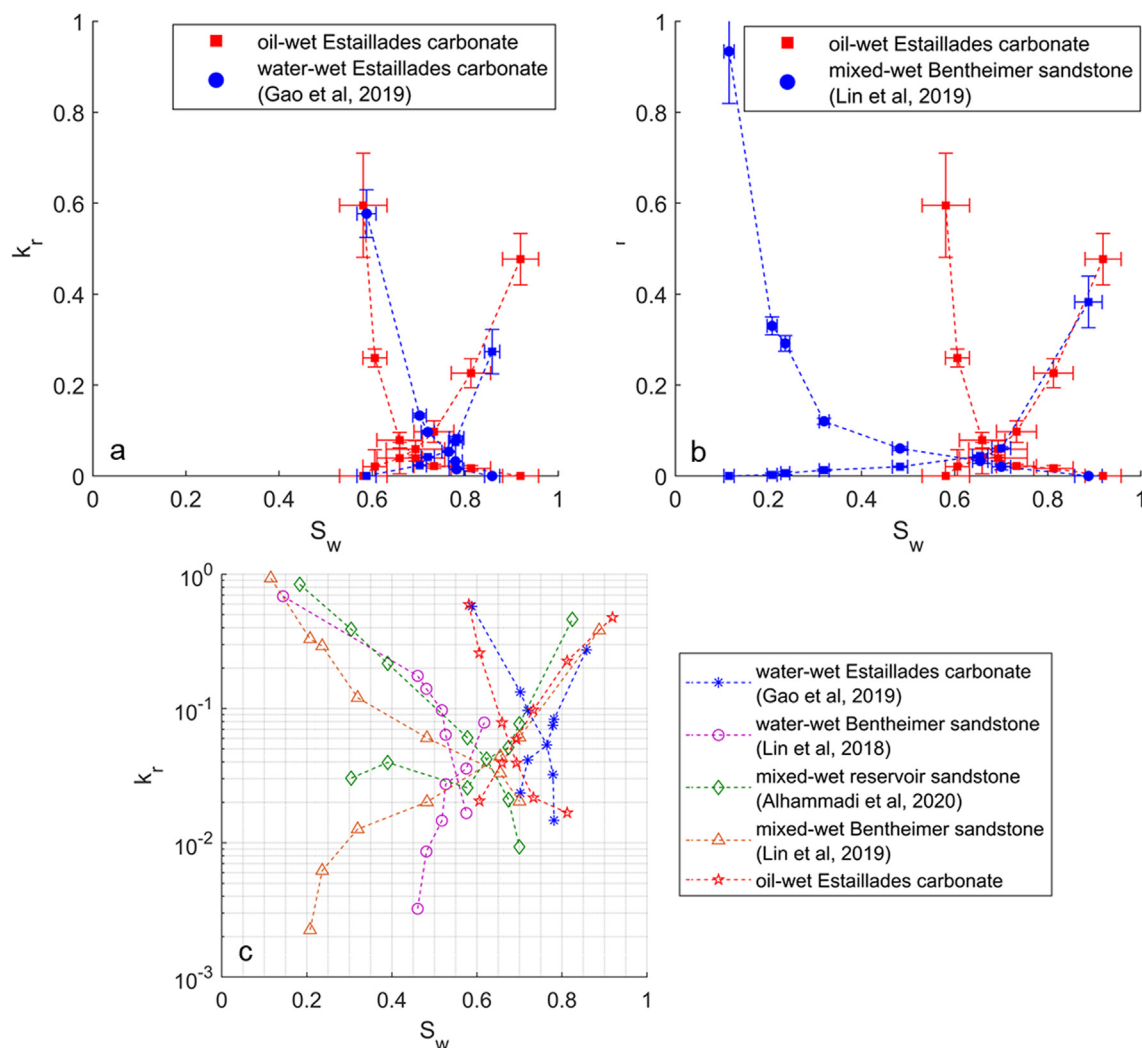

Fig. 12. The recorded differential pressure across core at steady state for 2 h before starting the scan at each fractional flow. The mean pressure differential and standard deviation are shown.

Fig. 13. Waterflood relative permeabilities at steady state for the altered-wettability Estaillades carbonate measured in this study. The result is compared to the previously published measurements on water-wet and mixed-wet Bentheimer sandstone, a water-wet Estaillades sample and a mixed-wet reservoir carbonate where the relative permeability is shown on a logarithmic axis (Alhammadi et al., 2020; Gao et al., 2019; Lin et al., 2019b, 2019a, 2018).

the sample, but these larger pores only connected through the pore space at a high brine saturation. This led to a low brine relative permeability. The behaviour we have observed for our altered-wettability carbonate is distinct, for the same two reasons discussed for the sandstone. Firstly, in the reservoir sample the wettability alteration was less strong, with thermodynamic contact angles that varied from 20° to just below 120° as the fractional flow increased: the sample was more mixed-wet than uniformly oil-wet in the macro pore space. Secondly, the micro-porosity only constituted one third of the total porosity, not 60% as in our case. As a consequence, the flow between macro pores through micro-porosity had less impact on the relative permeability: micro-porosity provided water for filling but did not substantially contribute to the flow conductance.

Overall, the flow behaviour encapsulated in the relative permeability is a subtle combination of pore structure, connectivity and wettability. In our altered-wettability carbonate we have a poorly-connected oil-wet macro pore space. Filling of the larger pores, combined with additional connectivity provided through micro-porosity, led to a sharp rise in the brine relative permeability implying poor recovery, consistent with the analysis of curvature and connectivity.

4. Conclusions and outlook

In this study, we have presented measurements of relative permeability combined with pore-scale imaging for a micro-porous Estaillades carbonate whose wettability had been altered through contact with crude oil. We introduced an alternative image analysis method which provides an accurate measurement of saturation directly from grey-scale micro-CT images without performing image segmentation which could be uncertain for systems containing large amount of sub-resolution pores containing both oil and brines phases. Pore-scale imaging also provides accurate measurements of interfacial properties, including interfacial area, curvatures, and thermodynamic contact angles.

We compared the behaviour with previously published results on a water-wet Estaillades carbonate and on a Bentheimer sandstone which had also been in contact with crude oil. Our altered-wettability Estaillades displayed oil-wet characteristics with a lower oil relative permeability, higher water relative permeability and lower residual oil saturation ($S_{or} = 0.08$) than in the water-wet case ($S_{or} = 0.14$) and mixed-wet Bentheimer case ($S_{or} = 0.11$).

The oil-wet nature of the sample was confirmed by the calculation of contact angle from energy balance which gave a value of approximately 120°, as opposed to 95° for the sandstone. This result was consistent with the lower, more negative capillary pressure in the carbonate (see Table 1) and an analysis of the sequence of pore filling. In the carbonate, displacement first occurred preferentially in the larger pores, as expected for an oil-wet system, whereas elements of all size were filled throughout the displacement for the mixed-wet sandstone.

In comparison with Bentheimer sandstone, Estaillades carbonate has a much poorer connected macro pore space; connectivity is mainly maintained through sub-resolution micro-porosity. In the carbonate, locally either oil or brine almost fully occupied the macro pore space, where the brine fraction in the pore space is either lower than 10% or higher than 90%, at the resolution of the image, in contrast to the sandstone where both phases could be present as layers close to the surface or, in the case of oil, sandwiched between brine near the surface and brine in the centre of the pore. In the carbonate there was also oil initially in the sub-resolution micro porosity which was displaced during waterflooding.

Overall, the carbonate we studied has two features which distinguish it from the sandstones studied hitherto. Firstly, the larger (macro) pore space is more oil-wet, where the larger pores are filled first during brine injection, giving a large and negative capillary pressure. Secondly, micro-porosity, below the resolution of the images, contributes 60% to the total porosity. The macro pore space is poorly connected, but micro-porosity provides additional connectivity, particularly for the brine. This leads to a brine relative permeability that rises sharply with brine saturation and implies rather poor recovery efficiency.

Future work could extend this workflow to a wider range of samples under different wettability conditions, as well as using the results as a benchmark for calibration and validation of pore-scale models (Bultreys et al., 2018; Foroughi et al., 2020).

CRediT authorship contribution statement

Qingyang Lin: Conceptualization, Methodology, Investigation, Data curation, Formal analysis, Writing - original draft. **Branko Bijeljic:** Conceptualization, Methodology, Investigation, Supervision, Writing - original draft. **Sajjad Foroughi:** Investigation, Data curation, Formal analysis, Writing - review & editing. **Steffen Berg:** Conceptualization, Investigation, Writing - review & editing. **Martin J. Blunt:** Conceptualization, Methodology, Investigation, Formal analysis, Supervision, Writing - original draft.

Declaration of Competing Interest

The authors declare that they have no known competing financial interests or personal relationships that could have appeared to influence the work reported in this paper.

Data availability

All the image data used in this work are available at the Digital Rocks Portal: https://doi.org/10.17612/xwvw-9e52.

References

Akai, T., Lin, Q., Bijeljic, B., Blunt, M.J., 2020. Using energy balance to determine pore-scale wettability. J. Colloid Interface Sci. 576, 486–495. https://doi.org/10.1016/j.jcis.2020.03.074.

Al-Khulaifi, Y., Lin, Q., Blunt, M.J., Bijeljic, B., 2017. Reaction rates in chemically heterogeneous rock: coupled impact of structure and flow properties studied by X-ray microtomography. Environ. Sci. Technol. 51, 4108–4116. https://doi.org/10.1021/acs.est.6b06224.

Alhammadi, A.M., Gao, Y., Akai, T., Blunt, M.J., Bijeljic, B., 2020. Pore-scale X-ray imaging with measurement of relative permeability, capillary pressure and oil recovery in a mixed-wet micro-porous carbonate reservoir rock. Fuel 268,. https://doi.org/10.1016/j.fuel.2020.117018 117018.

Alhosani, A., Scanziani, A., Lin, Q., Foroughi, S., Alhammadi, A.M., Blunt, M.J., Bijeljic, B., 2020. Dynamics of water injection in an oil-wet reservoir rock at subsurface conditions: Invasion patterns and pore-filling events. Phys. Rev. E 102,. https://doi.org/10.1103/PhysRevE.102.023110 023110.

AlRatrout, A., Blunt, M.J., Bijeljic, B., 2018. Wettability in complex porous materials, the mixed-wet state, and its relationship to surface roughness. Proc. Natl. Acad. Sci. 115, 8901–8906. https://doi.org/10.1073/pnas.1803734115.

AlRatrout, A., Raeini, A.Q., Bijeljic, B., Blunt, M.J., 2017. Automatic measurement of contact angle in pore-space images. Adv. Water Resour. 109, 158–169. https://doi.org/10.1016/j.advwatres.2017.07.018.

Andreas, J.M., Hauser, E.A., Tucker, W.B., 1937. Boundary tension by pendant drops 1. J. Phys. Chem. 42, 1001–1019. https://doi.org/10.1021/j100903a002.

Andrew, M., Bijeljic, B., Blunt, M.J., 2014a. Pore-scale contact angle measurements at reservoir conditions using X-ray microtomography. Adv. Water Resour. 68, 24–31. https://doi.org/10.1016/j.advwatres.2014.02.014.

Andrew, M., Bijeljic, B., Blunt, M.J., 2014b. Pore-by-pore capillary pressure measurements using X-ray microtomography at reservoir conditions: Curvature, snap-off, and remobilization of residual CO2. Water Resour. Res. 50, 8760–8774. https://doi.org/10.1002/2014WR015970.

Armstrong, R.T., Pentland, C.H., Berg, S., Hummel, J., Lichau, D., Bernard, L., 2012a. Estimation of curvature from micro-CT liquid-liquid displacement studies with pore scale resolution SCA2012-55 Int. Symp. Soc. Core Anal., 6

Armstrong, R.T., Porter, M.L., Wildenschild, D., 2012b. Linking pore-scale interfacial curvature to column-scale capillary pressure. Adv. Water Resour. 46, 55–62. https://doi.org/10.1016/j.advwatres.2012.05.009.

Berg, S., Ott, H., Klapp, S.A., Schwing, A., Neiteler, R., Brussee, N., Makurat, A., Leu, L., Enzmann, F., Schwarz, J.-O., Kersten, M., Irvine, S., Stampanoni, M., 2013. Real-time 3D imaging of Haines jumps in porous media flow. Proc. Natl. Acad. Sci. 110, 3755–3759.

Berger, M., Levy, S., Gostiaux, B., 2012. Differential Geometry: Manifolds, Curves, and Surfaces: Manifolds, Curves, and Surfaces, Graduate Texts in Mathematics. Springer, New York.

Blunt, M.J., 2017. Multiphase Flow in Permeable Media. Cambridge University Press, Cambridge, United Kingdom. Doi: 10.1017/9781316145098.

Blunt, M.J., Akai, T., Bijeljic, B., 2020. Evaluation of methods using topology and integral geometry to assess wettability. J. Colloid Interface Sci. 576, 99–108. https://doi.org/10.1016/j.jcis.2020.04.118.

Blunt, M.J., Lin, Q., Akai, T., Bijeljic, B., 2019. A thermodynamically consistent characterization of wettability in porous media using high-resolution imaging. J. Colloid Interface Sci. 552, 59–65. https://doi.org/10.1016/j.jcis.2019.05.026.

Boone, M.A., De Kock, T., Bultreys, T., De Schutter, G., Vontobel, P., Van Hoorebeke, L., Cnudde, V., 2014. 3D mapping of water in oolithic limestone at atmospheric and vacuum saturation using X-ray micro-CT differential imaging. Mater. Charact. 97, 150–160. https://doi.org/10.1016/j.matchar.2014.09.010.

Buades, A., Coll, B., Morel, J.-M., 2008. Nonlocal image and movie denoising. Int. J. Comput. Vis. 76, 123–139. https://doi.org/10.1007/s11263-007-0052-1.

Bultreys, T., Lin, Q., Gao, Y., Raeini, A.Q., AlRatrout, A., Bijeljic, B., Blunt, M.J., 2018. Validation of model predictions of pore-scale fluid distributions during two-phase flow. Phys. Rev. E 97,. https://doi.org/10.1103/PhysRevE.97.053104 053104.

Culligan, K.A., Wildenschild, D., Christensen, B.S.B., Gray, W.G., Rivers, M.L., 2006. Pore-scale characteristics of multiphase flow in porous media: A comparison of air–water and oil–water experiments. Adv. Water Resour. 29, 227–238. https://doi.org/10.1016/j.advwatres.2005.03.021.

Dong, H., Blunt, M.J., 2009. Pore-network extraction from micro-computerized-tomography images. Phys. Rev. E 80, 36307.

Foroughi, S., Bijeljic, B., Lin, Q., Raeini, A.Q., Blunt, M.J., 2020. Pore-by-pore modeling, analysis, and prediction of two-phase flow in mixed-wet rocks. Phys. Rev. E 102,. https://doi.org/10.1103/PhysRevE.102.023302 023302.

Gao, Y., Lin, Q., Bijeljic, B., Blunt, M.J., 2017. X-ray microtomography of intermittency in multiphase flow at steady state using a differential imaging method. Water Resour. Res. 53, 10274–10292. https://doi.org/10.1002/2017WR021736.

Gao, Y., Qaseminejad Raeini, A., Blunt, M.J., Bijeljic, B., 2019. Pore occupancy, relative permeability and flow intermittency measurements using X-ray micro-tomography in a complex carbonate. Adv. Water Resour. 129, 56–69. https://doi.org/10.1016/j.advwatres.2019.04.007.

Garing, C., de Chalendar, J.A., Voltolini, M., Ajo-Franklin, J.B., Benson, S.M., 2017. Pore-scale capillary pressure analysis using multi-scale X-ray micromotography. Adv. Water Resour. 104, 223–241. https://doi.org/10.1016/j.advwatres.2017.04.006.

Gauss, K.F., Pesic, P., 2005. General Investigations of Curved Surfaces, Dover Books on Mathematics. Dover Publications.

Jackson, S.J., Lin, Q., Krevor, S., 2020. Representative elementary volumes, hysteresis, and heterogeneity in multiphase flow from the pore to continuum scale. Water Resour. Res. 56. https://doi.org/10.1029/2019WR026396.

Jones, A.C., Arns, C.H., Sheppard, A.P., Hutmacher, D.W., Milthorpe, B.K., Knackstedt, M.A., 2007. Assessment of bone ingrowth into porous biomaterials using micro-CT. Biomaterials 28, 2491–2504. https://doi.org/10.1016/j.biomaterials.2007.01.046.

Leu, L., Berg, S., Enzmann, F., Armstrong, R.T., Kersten, M., 2014. Fast X-ray micro-tomography of multiphase flow in Berea sandstone: a sensitivity study on image processing. Transp. Porous Media 105, 451–469. https://doi.org/10.1007/s11242-014-0378-4.

Li, T., Schlüter, S., Dragila, M.I., Wildenschild, D., 2018. An improved method for estimating capillary pressure from 3D microtomography images and its application to the study of disconnected nonwetting phase. Adv. Water Resour. 114, 249–260. https://doi.org/10.1016/j.advwatres.2018.02.012.

Lin, Q., Al-Khulaifi, Y., Blunt, M.J., Bijeljic, B., 2016. Quantification of sub-resolution porosity in carbonate rocks by applying high-salinity contrast brine using X-ray microtomography differential imaging. Adv. Water Resour. 96, 306–322. https://doi.org/10.1016/j.advwatres.2016.08.002.

Lin, Q., Alhammadi, A.M., Gao, Y., Bijeljic, B., Blunt, M.J., 2019a. iSCAL for Complete Rock Characterization: Using Pore-Scale Imaging to Determine Relative Permeability and Capillary Pressure. In: SPE Annual Technical Conference and Exhibition. Society of Petroleum Engineers. Doi: 10.2118/196082-MS

Lin, Q., Bijeljic, B., Berg, S., Pini, R., Blunt, M.J., Krevor, S., 2019b. Minimal surfaces in porous media: Pore-scale imaging of multiphase flow in an altered-wettability Bentheimer sandstone. Phys. Rev. E 99,. https://doi.org/10.1103/PhysRevE.99.063105 063105.

Lin, Q., Bijeljic, B., Krevor, S.C., Blunt, M.J., Rücker, M., Berg, S., Coorn, A., Van Der Linde, H., Georgiadis, A., Wilson, O.B., 2019c. A new waterflood initialization protocol with wettability alteration for pore-scale multiphase flow experiments. Petrophys. – SPWLA J. Form. Eval. Reserv. Descr. 60, 264–272. https://doi.org/10.30632/PJV60N2-2019a4.

Lin, Q., Bijeljic, B., Pini, R., Blunt, M.J., Krevor, S., 2018. Imaging and measurement of pore-scale interfacial curvature to determine capillary pressure simultaneously with relative permeability. Water Resour. Res. 54, 7046–7060. https://doi.org/10.1029/2018WR023214.

Lin, Q., Bijeljic, B., Rieke, H., Blunt, M.J., 2017. Visualization and quantification of capillary drainage in the pore space of laminated sandstone by a porous plate method using differential imaging X-ray microtomography. Water Resour. Res. 53, 7457–7468. https://doi.org/10.1002/2017WR021083.

Morrow, N., Buckley, J., 2011. Improved oil recovery by low-salinity waterflooding. J. Pet. Technol. 63, 106–112. https://doi.org/10.2118/129421-JPT.

Pak, T., Butler, I.B., Geiger, S., van Dijke, M.I.J., Sorbie, K.S., 2015. Droplet fragmentation: 3D imaging of a previously unidentified pore-scale process during multiphase flow in porous media. Proc. Natl. Acad. Sci. 112, 1947–1952. https://doi.org/10.1073/pnas.1420202112.

Prodanović, M., Lindquist, W.B., Seright, R.S., 2004. 3D microtomographic study of fluid displacement in rock cores. pp. 223–234. Doi: 10.1016/S0167-5648(04)80052-2

Raeini, A.Q., Bijeljic, B., Blunt, M.J., 2017. Generalized network modeling: Network extraction as a coarse-scale discretization of the void space of porous media. Phys. Rev. E 96,. https://doi.org/10.1103/PhysRevE.96.013312 013312.

Saxena, N., Hofmann, R., Alpak, F.O., Dietderich, J., Hunter, S., Day-Stirrat, R.J., 2017. Effect of image segmentation & voxel size on micro-CT computed effective transport & elastic properties. Mar. Pet. Geol. 86, 972–990. https://doi.org/10.1016/j.marpetgeo.2017.07.004.

Scanziani, A., Lin, Q., Alhosani, A., Blunt, M.J., Bijeljic, B., 2020. Dynamics of fluid displacement in mixed-wet porous media. Proc. R. Soc. A Math. Phys. Eng. Sci. 476, 20200040. https://doi.org/10.1098/rspa.2020.0040.

Schlüter, S., Sheppard, A., Brown, K., Wildenschild, D., 2014. Image processing of multiphase images obtained via X-ray microtomography: A review. Water Resour. Res. 50, 3615–3639. https://doi.org/10.1002/2014WR015256.

Singh, K., Menke, H., Andrew, M., Lin, Q., Rau, C., Blunt, M.J., Bijeljic, B., 2017. Dynamics of snap-off and pore-filling events during two-phase fluid flow in permeable media. Sci. Rep. 7, 5192. https://doi.org/10.1038/s41598-017-05204-4.

Soulaine, C., Gjetvaj, F., Garing, C., Roman, S., Russian, A., Gouze, P., Tchelepi, H.A., 2016. The impact of sub-resolution porosity of X-ray microtomography images on the permeability. Transp. Porous Media 113, 227–243. https://doi.org/10.1007/s11242-016-0690-2.

Stauffer, C.E., 1965. The measurement of surface tension by the pendant drop technique. J. Phys. Chem. 69, 1933–1938. https://doi.org/10.1021/j100890a024.

Sun, C., McClure, J.E., Mostaghimi, P., Herring, A.L., Berg, S., Armstrong, R.T., 2020. Probing effective wetting in subsurface systems. Geophys. Res. Lett. 47. https://doi.org/10.1029/2019GL086151.

Taubin, G., 1995. Curve and surface smoothing without shrinkage. In: Proceedings of IEEE International Conference on Computer Vision. IEEE Comput. Soc. Press, pp. 852–857. Doi: 10.1109/ICCV.1995.466848